Evaporation of bi-component droplets in a highly turbulent channel flow

Adrien Jean, Rudy Bazile, Bernard Ferret

EVAPORATION OF BI-COMPONENT DROPLETS IN A HIGHLY TURBULENT CHANNEL FLOW

Adrien Jean,* **Rudy Bazile, Bernard Ferret**

Institut de Mécanique des Fluides de Toulouse, Allée pr. Camille Soula, 31400, Toulouse, France
Université de Toulouse, Toulouse, France

ABSTRACT

To better understand the phenomena that occur in a jet engine combustion chamber where multi-component fuel droplets are injected, the influence of the fuel composition upon the liquid droplets' behavior in a turbulent air flow is investigated experimentally. In particular, the effect of the presence of an alcohol in the fuel is explored. A model experiment has been designed purposely, which enables to create in a canal a heated, highly turbulent air flow with good properties of homogeneous and isotropic turbulence, and yet with high levels of turbulent fluctuations. A spray of poly-dispersed bi-component acetone/ethanol fuel droplets is injected coaxially in the established zone of the air flow. The large range of droplet sizes ensures that they have a wide variety of behaviors with regard to turbulence. An optical access allows the observation of the turbulent two-phase flow and its evolution in the channel. Measurement campaigns are conducted using Planar Laser-Induced Fluorescence to characterize the droplets' evaporation regimes. Instantaneous acetone vapor concentrations are extracted from these measurements and it is found that acetone evaporates faster from bi-component droplets as compared with pure acetone droplets.

KEY WORDS: Spray and atomization, Two-phase flow, Turbulent transport, Evaporation, Bi-component droplets, Laser-Induced Fluorescence.

1. INTRODUCTION

In the actual framework of reducing pollutant emissions and improve the performance of aeronautical combustion chambers, phenomena linked to injection, vaporization, and mixing of multi-component fuels are to be understood so as to improve predictions of combustion. Extensive research has been carried out in the field to explore and model the droplet heating and vaporization process, since it is of great importance to dispose of accurate, flexible and low computational cost evaporation models that can be implemented in CFD codes (Bodoc et al. (2013)).

These models are generally based on the assumption of a single component fuel. However according to Maqua et al. (2008) this simplification is difficult to trust since the vaporization of multi-component droplets exhibits additional complex features. Models accounting for the multi-component nature of the fuel are usually based on the discrete component approach and remain applicable only when a small number of components are involved, whereas real fuels contain hundreds of chemical species.

To address the lack of experimental data concerning the evaporation of multi-component droplets, a model

experiment for the study of the evaporation of a mist of polydispersed droplets in a highly turbulent, homogeneous and isotropic heated flow of air is available at IMFT that enables to reproduce flows encountered in aeronautical combustion chambers, where sprays of polydispersed multi-component fuel droplets are generated. The present paper is focused on bi-component fuel droplets made of acetone and ethanol.

Measurement campaigns are conducted using Planar Laser-Induced Fluorescence (PLIF) to characterize the droplets' evaporation regimes. Instantaneous acetone vapor concentrations are extracted from these measurements. In the present paper, the experimental set-up and the PLIF set-up for the vapor concentration measurements are first presented; then the results concerning the carrier flow, the evaporation of pure acetone droplets and that of binary droplets are exposed and discussed; conclusions are formulated.

2. EXPERIMENTAL SET-UP

In order to study the evaporation of a droplet mist in turbulent conditions, we use a system of turbulence generator developed by Videto and Santavicca (1991) which allows turbulence levels up to 40% with good isotropic behavior. This system is based on the observation of automotive engines internal aerodynamics and consists in a perforated plate located at the entrance of a contraction which leads into a channel. The orifices in the plate are holes located near the contraction walls. Air flows through these orifices creating vortexes that impact the walls and get mixed while entering the channel. Their high scale energy is then transformed into turbulent kinetic energy which relative level is higher than for grid turbulence. Several authors have used this system. In particular, Bédat and Cheng (1995) found relative turbulence intensity of about 30% to 40% for a large range of air mass flow rate and a good isotropy on a large portion of the flow.

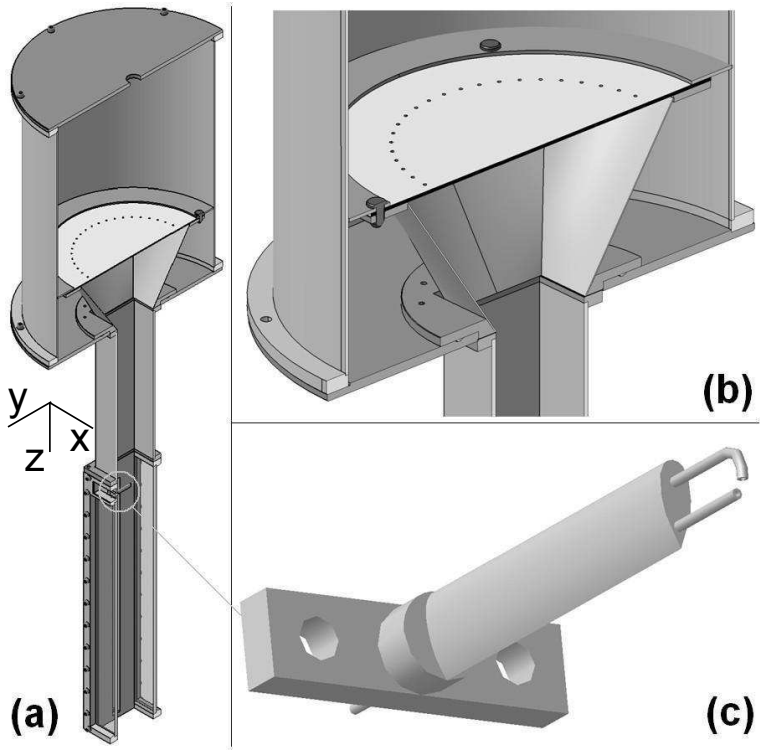

Fig. 1 Experimental set-up: (a) general view, (b) turbulence generator and (c) air-blast injection device.

The experimental configuration was adapted to our needs and is described in previous works: Cochet et al. (2009), Moreau and Bazile (2012). The orifices are forty-five 3 mm diameter holes located on a perimeter near the constriction walls. A circle-square convergent connects the perforated plate and the cylindrical reservoir to a square-shaped channel. Fig. 1 (a) provides a schematic representation of the entire test bench, while Fig. 1

(b) focuses on the turbulence generator. The channel has a $H^2 = 92 \times 92$ mm^2 cross-section and is composed of a blind segment and an optical segment equipped with two narrow quartz windows and two wide Pyrex windows allowing optical measurements along a large portion ($\approx 5H$ long) of the channel. The z axis is the longitudinal axis and the x and y axes are the radial axes; their origin is taken at the injection point. In the following sections, most results will be given versus x/H and z/H.

With a mean flow velocity of $W_0 = 2$ m/s, expected turbulence levels of about 25% $4H$ after the entrance of the channel and integral length scales of about 20 mm, we can expect a turbulent Reynolds number in the range of 550. The carrier flow is heated thanks to an Osram heating resistance at $T_{air} = 373$ K. The test bench is insulated so as to prevent heat losses.

Two cases of liquid composition are considered in this study: one is pure acetone, referred to as the *mono-component case* in the following ; the second case is a mix of acetone and ethanol ($50\% - 50\%$ in mass) and is hereinafter referred to as the *bi-component case*. Properties of acetone and ethanol are summarized Table 1.

Table 1 Some properties of acetone and ethanol.

Chemical compound	Acetone	Ethanol
Formula	CH_3COCH_3	CH_3CH_2OH
Molar mass [g/mol]	58.08	46.07
Density [kg/m^3]	791	789
Boiling temperature [K]	330	352
Vapor pressure at 293 K / 20°C [kPa]	25.6	5.8

In order to create the droplet mist, an air-blast atomizer made of two steel needles (500 µm inner diameter) is used, as shown Fig. 1 (c). A high velocity air jet coming from the upper, $90°$-bent needle impinges on and breaks the liquid jet exiting the lower needle at the *injection point*, creating a spray of fine droplets. According to Lazaro and Lasheras (1989), this design introduces small disturbances and adds a very small amount of turbulent energy to the base flow. The injection device is mounted right in the middle of the channel's cross-section and $4H = 368$ mm from its entrance. The choice of this distance is driven by the characteristics of the carrier flow (see section 4.1), which is established at a distance of $\approx 4H$ after the entrance of the channel; as a result the initial conditions of the two-phase flow (i.e. at the injection point) are well controlled.

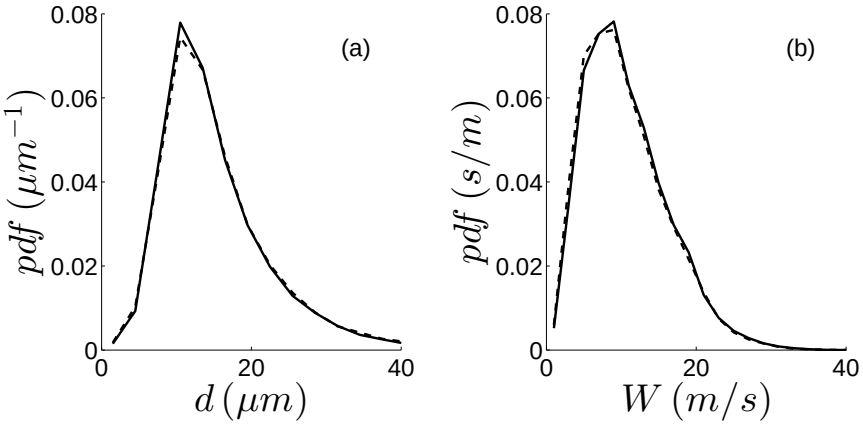

Fig. 2 Initial conditions of the spray: (a) size and (b) axial velocity distributions of droplets for two fuel mixtures: pure acetone (solid line) and acetone-ethanol (dashed line).

Initial properties of the spray were measured in quiescent air and at room temperature using Phase-Doppler Anemometry. Figure 2 shows for the two liquid compositions the droplets (a) size d and (b) axial velocity W distributions in the spray, in a measuring volume located $z = 20$ mm downstream the injection point.

The distributions superpose very well: there is no significant difference between the two cases for the spray's initial conditions. The largest droplets do not exceed 50 µm in diameter: the evaporation coefficient of acetone droplets in equilibrium with the carrier flow at $W_0 = 2$ m/s gives an estimation of the distance such droplets can run before complete evaporation (d^2-law, Spalding (1951)), namely $\approx 3H$. The length of the channel's optical segment ($5H$) was chosen accordingly to make sure the whole evaporation zone is covered.

Mean arithmetic diameter d_{10} is of approximately 15.5 µm, while Sauter mean diameter d_{32} is of about 27 µm. Droplets have and average axial velocity of 9.5 m/s. In order to have an idea of the droplets behavior, Stokes number based on integral and Kolmogorov length scales are computed for the droplets mean diameters:

$$St_L = \tau_p/T_e \qquad \text{and} \qquad St_k = \tau_p/\tau_k \tag{1}$$

with τ_p the droplets' relaxation time, $T_e = 51$ ms the integral time scale of the carrier flow and $\tau_k = 2.2$ ms the characteristic time of the Kolmogorov scale. Table 2 shows different values of Stokes numbers for several droplet sizes. Droplets of the spray have a rather large range of Stokes number. The smallest ones should follow the different structures of the flow while the largest ones should only follow the most energetic scales of turbulence.

Table 2 Stokes numbers for various droplet size classes.

Droplet size [µm]	5	10	25	50
St_L	0.002	0.035	1.12	14.4
St_k	0.057	0.83	26.4	340

3. PLIF SET-UP FOR VAPOR CONCENTRATION MEASUREMENTS

Planar Laser Induced Fluorescence (PLIF) is used to measure instantaneous acetone vapor concentration fields. Laser Induced Fluorescence is based on the physical phenomenon of fluorescence, first discovered by Jablonski: when certain molecules are excited by a laser beam, they emit a fluorescence signal with a higher wavelength than the excitation light, thus allowing discrimination between excitation and emission lights. Since the number of emitted photons is proportional to the number of excited molecules it is possible to have a direct measurement of the number density N. Indeed, the fluorescence signal (as a function of the path length x in a fluorescent medium) is written:

$$S_f(x) = I(x) \cdot \phi_\lambda^f(\lambda, T, P, N) \cdot N(x) \cdot \sigma(\lambda, T) \tag{2}$$

In this equation, I is the laser energy, $\sigma = 4.36 \times 10^{-24}$ m^2/molecule is the absorption cross section, λ the incident laser wavelength, ϕ_λ^f the fluorescence quantum yield, P the pressure and T the temperature. When λ is fixed and P and T do not vary much, $S_f(x)$ depends only on N.

Since liquid is much more dense than vapor by a ratio of about 1000, its fluorescence signal should also be more intense by the same ratio and intensified cameras do not have a strong enough dynamic to safely record both kinds of signal. Either the signal from the droplets will saturate the intensified camera, or the vapor signal will be below noise level. A solution, suggested by Bazile and Stepowski (1995), consists in using a molecule with a strong absorption coefficient in order to make drops fluorescence limited to a surface contribution while the contribution of the gas phase scales as the mass of vapor. The necessary camera dynamic is thus reduced and vapor phase concentration can be obtained in regions where liquid is diluted enough.

In this experiment, the fluorescent liquid is acetone; ethanol does not fluoresce so as not to disturb the signal. According to Thurber and Hanson (1999), acetone has a high saturation pressure and a good fluorescence yield (0.2% at 266 nm). Moreover, its strong absorption coefficient at the laser wavelength and its low dependence

of fluorescence properties on pressure and temperature (constant quenching) makes it ideal for studies under various thermal conditions.

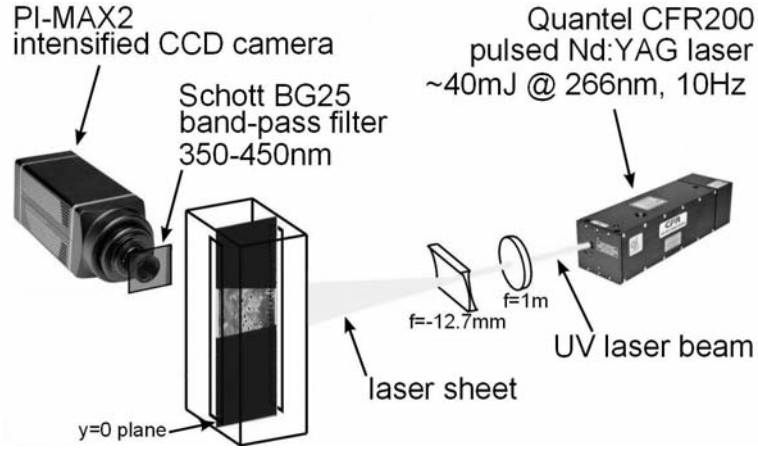

Fig. 3 Planar Laser-Induced Fluorescence set-up.

Figure 3 shows the test bench with the laser and the camera used for PLIF measurements. A Nd:YAG laser produces a beam filtered by a dichroic mirror to reflect only the ultraviolet light. The UV laser beam is then stretched into a thin sheet ($\lambda = 266$ nm,$\Delta t = 10$ ns, $I_0 \approx 40$ mJ, 400 µm thick) by a diverging, cylindrical lens and focused on the symmetry plane of the optical segment through the two narrow quartz windows. An intensified CCD camera (PI-MAX Princeton, 16 bits, 512×512 pixels^2) with a 58 mm $- f/1.2$ objective lens collects the fluorescence emission of the acetone droplets and vapor through the Pyrex window. The camera is equipped with a pass-band filter $BG25$ to remove Mie scattering from the droplets.

4. RESULTS AND DISCUSSION

4.1 Carrier flow

Results presented in this section are in good agreement with the work of Cochet et al. (2009) where details can be found. The characteristics of the carrier flow are only briefly summarized hereafter, and were obtained with Laser Doppler Velocimetry measurements for a flowing velocity of the carrier flow of $W_0 = 2$ m/s.

Instantaneous velocity components are the longitudinal velocity W and the radial velocity V. The turbulent velocity components w' and v' are defined as the standard deviations of instantaneous velocity fluctuations w and v:

$$w' = \sqrt{\overline{w^2}} = \sqrt{\overline{(W - \overline{W})^2}} \qquad \text{and} \qquad v' = \sqrt{\overline{v^2}} = \sqrt{\overline{(V - \overline{V})^2}} \tag{3}$$

There are three phases in the development of the channel flow. The first phase, from $z/H = -4$ to $z/H \approx -2.5$, corresponds to the *entrance zone* where $\overline{W}$ presents jet-like radial profiles and $\overline{W_{axis}} = \overline{W(x = y = 0)}$ decreases sharply. In the second phase called *transition zone*, $\overline{W_{axis}}$ decreases before reaching a minimum and increasing slowly. The mean velocity radial profiles are more wake-like and slowly tend towards homogenization, thus reaching the next zone at $z/H \approx 0$. In this third phase, the *established zone* ($z/H > 0$), radial profiles of the mean velocity $\overline{W}$ are very flat on more than 80% of the cross-section which indicates that the flow is highly homogeneous per section. Droplet injection is performed at the beginning of this zone of interest.

Figure 4 (a) shows the axial evolution of turbulent fluctuations of axial w' and radial v' velocities at the centerline ($x = y = 0$) of the channel, normalized by W_0. Turbulence levels decrease continuously through the channel but are very high since they reach around 25% at the beginning of the established zone. Furthermore

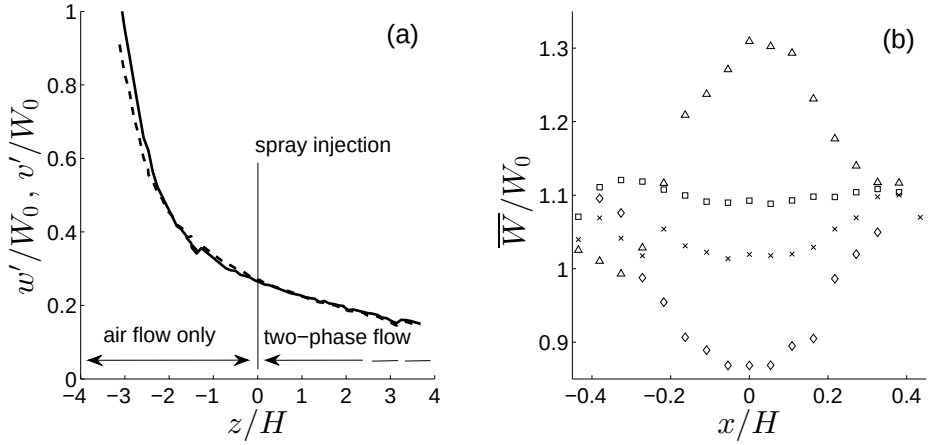

Fig. 4 Carrier flow: (a) axial evolution of rms fluctuations of axial (solid line) and radial (dashed line) velocities at the centerline of the channel, and (b) radial profiles of axial velocity ($y = 0$) at various axial locations: z/H=0.88 (triangle), z/H=2.01 (diamond), z/H=3.66 (cross) and z/H=4.75 (square).

the superposition of w'/W_0 and v'/W_0 shows a very good isotropy of the flow; the anisotropy coefficient ranges between 0.9 and 1.1.

Figure 4 (b) shows some radial profiles of mean axial velocity $\overline{W}$ normalized by W_0 at various axial locations in the channel. For small axial locations (entrance zone), $\overline{W}/W_0$ is higher int the center of the channel than close to the wall. The profiles are then inverted in the transition zone and tend to homogenize, to become almost flat in the established zone. This behavior is similar to what is observed for grid turbulence.

Besides, Reynolds stresses are very close to zero throughout a large part of the channel length, usually remaining under 5%. Results concerning skewness and flatness factors (respectively close to 0 and 3) tend to show that fluctuating velocities distributions are very close to Gaussian distributions, according to Cochet et al. (2009). All these elements point towards homogeneous and isotropic behavior with high turbulence levels in the established zone.

4.2 Evaporation

Results regarding the evaporation of droplets in the turbulent channel flow of heated air are presented in this section. The post processing of images is presented first, then results of the case of pure acetone droplets are exposed to enable the comparison with the bi-component (acetone-ethanol) case in the last sub-section.

4.2.1 Post processing of instantaneous fluorescent fields Information on mean and fluctuating acetone vapor concentrations can be extracted from instantaneous fluorescence images provided droplets are removed from the computations. This is made by an automated treatment of the row images which consists in detecting the liquid droplets and removing them. The discrimination method used here, previously described in Moreau and Bazile (2012) rely on the detection of high spatial frequencies. The raw image is first denoised, then filtered using a median filter. The filtered image is subtracted from the raw, denoised image. The result is an image containing the high spatial frequencies. After threshold and morphological treatments (erosion and dilatation), a binary image representing the shape of the droplets is obtained. The input image is multiplied by the negative of the binary image. The product is an image with information on the vapor phase only, as shown Fig. 5).

Far from the injection point ($z/H = 5$), the droplets are completely vaporized. The mean profile of acetone fluorescence is flat and corresponds to the maximum acetone vapor concentration, called C_∞, which can be

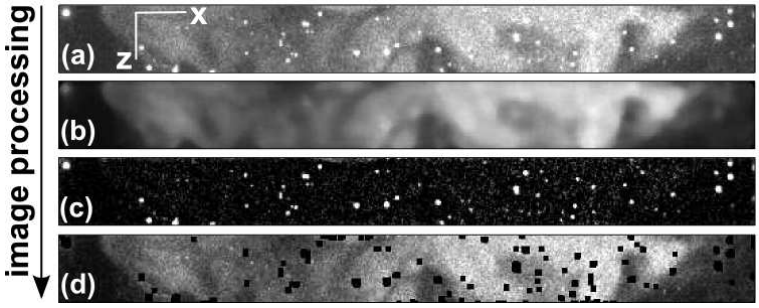

Fig. 5 Automated treatment of fluorescence images: (a) raw fluorescence image, (b) filtered image, (c) image of the high spatial frequencies and (d) vapor phase image.

computed:

$$C_\infty = \frac{\dot{m}_{acetone}}{W_0 H^2} \tag{4}$$

where $\dot{m}_{acetone}$ is the mass-flow of injected acetone. This is how the calibration of the fluorescent signal is performed. It follows that the concentration at a given axial z location is given by:

$$C(x) = C_\infty \cdot \frac{S_f(x)}{S_{f,\infty}} \tag{5}$$

where $S_{f,\infty}$ is the value of the fluorescent signal integrated over the mean profile at $z/H = 5.4$. In the bi-component case, the fuel mixture being equally composed of acetone and ethanol, C_∞ is half that in the mono-component case, as summarized in Table 3.

Table 3 Fuel parameters for the two studied experimental cases.

Case	Mono-component	Bi-component
Temperature	$T_{fuel} = 290$ [K] (room temperature)	
Liquid mass-flow rate	$\dot{m}_{fuel} = 0.21$ [g/s]	
Acetone mass fraction	$Y_{acetone} = 1$	$Y_{acetone} = 0.5$
Concentration far from injection	$C_\infty = 12.3$ [g/m^3]	$C_\infty = 6.15$ [g/m^3]

However, two corrections must be made. First, according to the Beer-Lambert law, light energy I in Eq. 2 is absorbed by the medium on its path and decreases exponentially:

$$I(x) = I_0 \cdot e^{-\sigma(\lambda) \int N(x) \mathrm{d}x} \tag{6}$$

where I_0 is the incident laser energy. The number density N is deduced from the mass vapor concentration C: $N = C \times \frac{N_A}{\overline{M}}$, where $N_A = 6.022 \times 10^{23}$ mol^{-1} is the Avogadro constant and $\overline{M}$ is the molar mass of the fluorescent medium, i.e. acetone. To correct this effect, the inverse operation is applied pixel by pixel to radial fluorescent profiles of acetone vapor, starting from the pixel closest to the laser source.

The second correction is to rectify the inhomogeneity of the light sheet, which is generated by a diverging lens, hence the light sheet itself is diverging and its energy is spread. We correct this by dividing the radial profiles by the one farthest from injection, $S_{f,\infty}$, supposed to be completely flat. All in all, these combined treatments account for a maximum 20% correction of the profile in the worst case (at axial locations far from injection and for the maximal path length, i.e. at $x/H \approx -0.5$, the laser source coming from the positive x).

After these two corrections, the radial profiles of acetone vapor concentration presented hereafter are symmetric. This tends to validate both the corrections and the non-standard calibration described above since the

number density term N given by the calibration is then used for the first correction (Eq. 6), which gives coherent results.

Moreover, in the worst case scenario (i.e. at z/H=1), the total droplets section (based on the mean Sauter diameter) crossing the laser source in the measurement volume is around 1% of the laser sheet section (thickness: 500 µm, height: 6.8 mm). Therefore the influence of the droplets on the laser absorption was not taken into account. All in all, uncertainties for the PLIF measurements presented in this study are in the range of 9%.

4.2.2 Mono-component case Figure 6 shows radial profiles (along x axis, $y = 0$) of acetone vapor concentration, normalized by C_∞, and its fluctuations and at various axial locations z in the channel. For small z, the concentration profiles have Gaussian shapes with a maximum concentration at the center of the channel and little vapor concentration close to the walls. The profiles flatten with z increasing, becoming almost flat at the last measured location $z/H = 4.9$ (f). These results were expected since at $z/H = 1$, i.e. close to the injection point, it is coherent that the vapor is concentrated at the center of the channel, while the vapor is spread across the channel's section with z increasing with the help of the turbulent carrier flow.

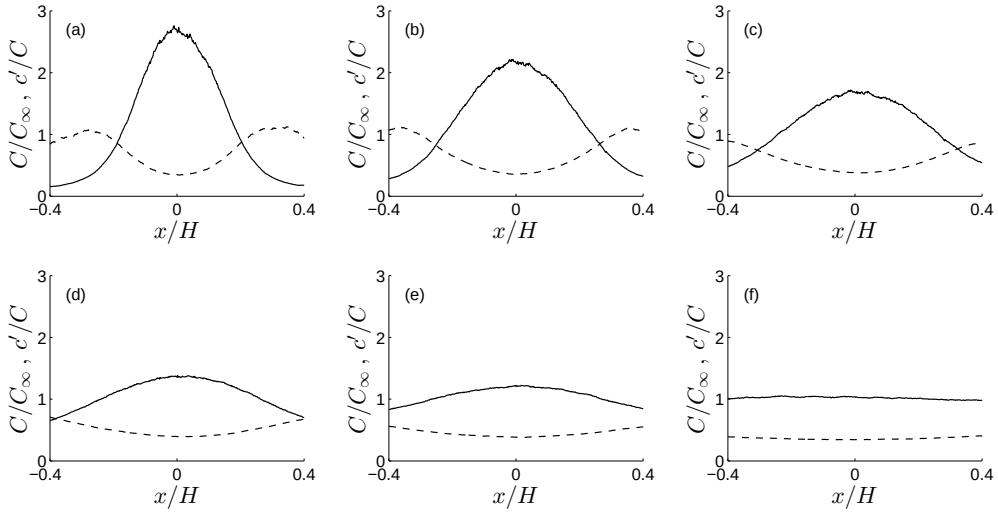

Fig. 6 Radial profiles of acetone vapor concentration (solid line) and its normalized RMS fluctuations (dashed line) at various axial locations: (a) $z/H = 1$, (b) $z/H = 1.6$, (c) $z/H = 2.3$, (d) $z/H = 3.1$, (e) $z/H = 3.6$ and (f) $z/H = 4.9$.

Figure 7 (a) shows the axial evolution of C_∞/C_{axis}, where $C_{axis} = C(x = y = 0, z)$ is the axial acetone vapor concentration. From $z/H = 1$ to $z/H = 3.6$, a strait line linear regression fits quite well the results, showing the hyperbolic dependence of C_{axis} upon z. A virtual origin z_0 can be computed from this regression, which value is given by the continuation of the line until it intersects the $x-$axis (at $z_0/H = -1.02$), meaning that the virtual origin of the spray is located at a distance $\sim H$ before its injection point.

Taking into account the virtual origin z_0 and making a variable substitution, one can show that the radial profiles of acetone vapor concentration visible Fig. 6 are self-preserving in the beginning of the spray's development: Figure 7 (b) shows the radial profiles, normalized by their maximum C_{max} (usually very close to C_{axis}), as a function of $x/(z - z_0)$ in lieu of x/H. The profile superimpose quite well from $z/H = 1$ to $z/H = 2.6$, showing the self-similarity of the spray. For $z/H > 2.6$, the presence of the walls prevents its self-similarity. A Gaussian profile (solid line) is shown for comparison, fitting the results quite well for a half-width at half-height of $b = 0.083z$.

This behavior is similar to what is observed in the development of free jets (gas as well as liquids) in both quiescent air and co-flow of air and for both velocity and concentration profiles. Fukushima et al. (2000) find

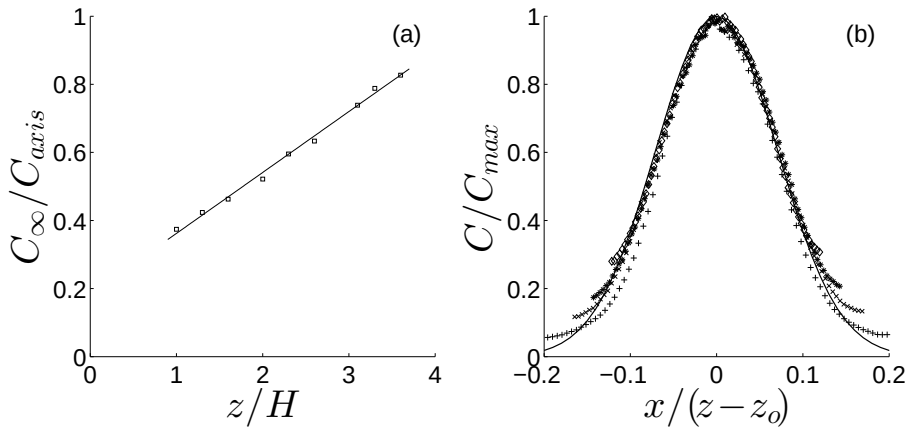

Fig. 7 (a) Axial evolution of the axial acetone vapor concentration and (b) profiles of acetone vapor concentration normalized by their maximum and as a function of $x/(z-z_o)$, at different axial locations: (plus) $z/H = 1$, (cross) $z/H = 1.6$, (asterisk) $z/H = 2$,(diamond) $z/H = 2.6$ and Gaussian fit (solid line).

a value of $b = 0.125z$ for the half-width of the concentration profiles. The difference is that in the present case there is a continuous production term of vapor after the injection and that the two-phase flow is confined. The interest of Fig 7 (a) and (b) is that one can reconstruct a radial profile of acetone concentration at any axial location (provided $z/H < 2.6$) downstream in the channel, from the value of C_{axis} at $z/H = 1$ and the coefficient of the slope (Fig 7 (a)) and the half-width b of the Gaussian fit (Fig 7 (b)). A parametric study is therefore conducted at $z/H = 1$ (see end of section 4.2.3) to help better understand the effect of dilution in the early development of the spray.

Normalized turbulent fluctuations of acetone vapor concentration c'/C give indication on the airvapor mixing: higher levels of fluctuation indicate a lower homogeneity of the mixing. From Fig. 6 (mainly (a), (b) and (c), i.e. for small z), it can be seen that c'/C is maximal at the border of the spray, at a radial location which gets closer to the wall as z increases. It is coherent since it is where the turbulent mixing takes place between the spray and the carrier flow. On the other hand, c'/C is minimal at the centerline of the channel but the difference is attenuated with increasing z as fluctuation profiles are homogenizing, indicating that acetone vapor is currently mixing with the air flow.

However, the fluctuations levels remain very high, invariably above 33% of C for all measured axial locations, meaning that the mixing is not perfectly realized, in spite of the flow being very turbulent. But as vaporization is still going on, there is still a production term for both vapor concentration and concentration fluctuations. Therefore, there are two phenomena competing since the first (the mixing) decreases fluctuations while the second (vapor production) increases them.

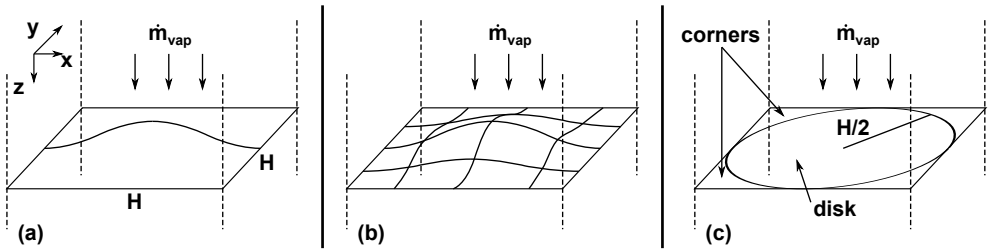

Fig. 8 Computing the acetone vapor mass-flow across the entire? cross-section of the channel (b) at a given axial z location, from the radial profile of acetone vapor concentration (a) at that location and an extrapolation of the profile at the corners (c).

The acetone vapor mass-flow $\dot{m}_{vap}(z)$ across the section of the channel (Fig. 8 (b)) at a given axial z location is written as the sum of the mass-flow through a disk of radius $H/2$ and that through the corners (Fig. 8 (c)):

$$\dot{m}_{vap}(z) = \dot{m}_{vap}^{disk}(z) + \dot{m}_{vap}^{corners}(z) \tag{7}$$

where $\dot{m}_{vap}^{disk}$ is computed by integrating the radial profile of acetone vapor concentration (Fig. 8 (a)) over the surface of the disk:

$$\dot{m}_{vap}^{disk}(z) = W_0 \iint^{disk} C(r,z)\,\mathrm{d}S \tag{8}$$

and $\dot{m}_{vap}^{corners}$ is estimated with the hypothesis that acetone vapor concentration through the corners is equal to the minimum of the radial profile.

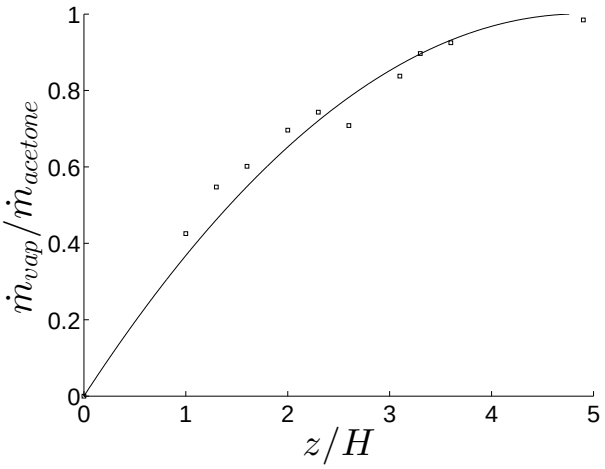

Fig. 9 Axial evolution of acetone vapor mass-flow through the channel cross-section, normalized by the injected liquid mass-flow (squares) and linear regression (solid line).

Figure 9 shows the axial evolution of acetone vapor mass-flow $\dot{m}_{vap}$ normalized by the injected liquid mass-flow of acetone $\dot{m}_{acetone}$. By $z/H = 1$, 40% of the injected acetone is vaporized; by $z/H = 3$, it is 80%. Therefore, the essential part of the evaporation process takes place before $z/H = 3$.

4.2.3 Bi-component case In this section dedicated to the bi-component case (50% acetone - 50% ethanol), the effect of the solvent (ethanol) on the vaporization of acetone is studied. All other parameters including camera settings such as intensification gain and diaphragm aperture are the same as in the mono-component case. Figure 10 shows radial ($y = 0$) profiles of acetone vapor concentration at different axial locations for the bi-component case. The profiles of the mono-component case seen Fig. 6 are shown again for comparison. The axial evolution of the profile has the same pattern as in the mono-component case with Gaussian profiles in the upper parts of the channel and almost flat ones far from injection.

However, the profiles of the bi-component case are consistently above that of the mono-component case: the relative acetone vapor concentration is higher at any given location for the former than for the latter case. This shows without doubt that the addition of ethanol in the fuel mixture accelerates the evaporation of acetone from the droplets. Such effect have been recently reported by Ammigan et al. (2012). In their study, bi-component acetone/ethanol droplets injected by a droplet generator travel through quiescent air and are exposed to asymmetric radiant heating. PLIF imaging of acetone vapor around the droplets indicates that the addition of ethanol promotes the cumulative vaporization of acetone despite the dilution in acetone concentration.

Figure 11 shows the axial evolution of axial concentration $C_{axis} = C(x = y = 0, z)$ normalized by C_∞: C_{axis}/C_∞ is maximal at $z/H = 1$, close to the injection point, and decreases towards 1 (asymptote) in both cases. However, axial concentration for the bi-component case is higher than for the mono-component case,

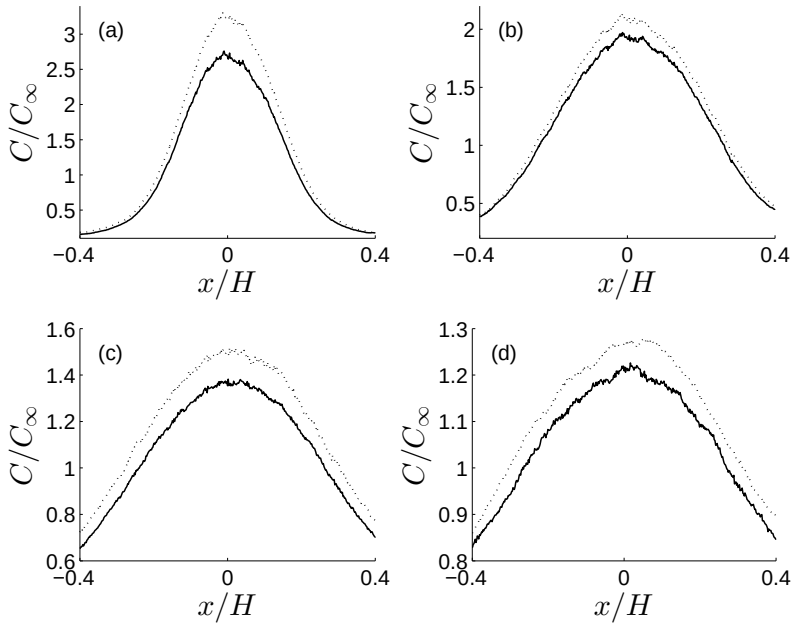

Fig. 10 Radial profiles of acetone vapor concentration from bi-component droplets (dotted line) at various axial locations: (a) $z/H = 1$, (b) $z/H = 2$, (c) $z/H = 3.1$, and (d) $z/H = 3.6$. Comparison with pure acetone droplets (solid line).

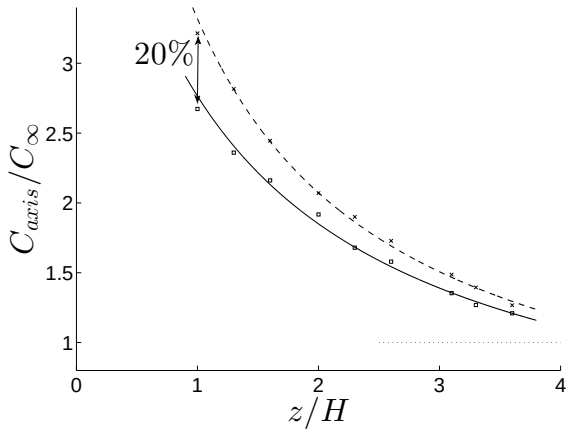

Fig. 11 Axial evolution of axial concentration: mono-component (square) and bi-component (cross) cases. Linear regressions (respectively solid and dashed lines) and asymptote (dotted line).

as one could guess from Fig. 10). The difference between the two cases is of 20% at $z/H = 1$ and then continuously decreases with z increasing, to reach 5% at $z/H = 3.6$. It is coherent with the fact that, far from the injection, the difference between the two cases becomes null as acetone is completely vaporized. However we noticed the presence of a few droplets at axial positions as high as $z/H = 5$. These droplets are almost exclusively composed of ethanol (the less volatile of the two components, see Table 1). This is confirmed by simulations of monodisperse stream of acetone/ethanol droplets using a code based on the effective diffusion model (Bodoc (2011)).

To further examine the effect of ethanol upon the vaporization of acetone, different cases of dilution of acetone in the fuel mixture (the rest being ethanol) are studied at $z/H = 1$ in the early development zone of the spray.

A parametric study is underway which first results are presented Fig. 12 but more are to come and will be exposed at IHTC.

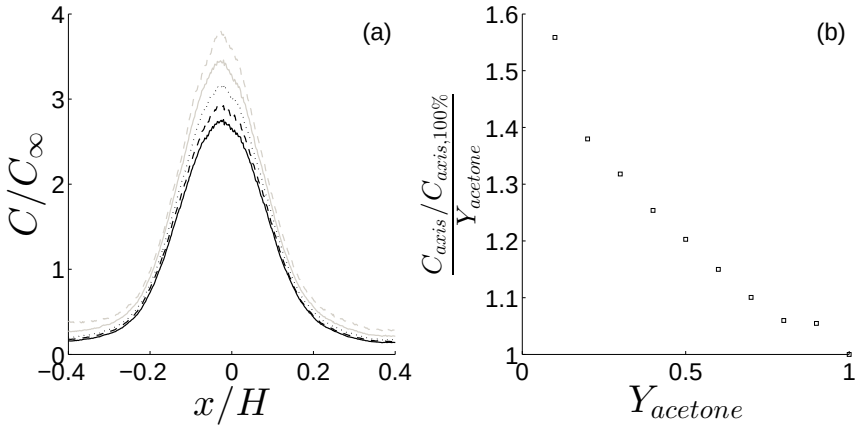

Fig. 12 Effect of droplet composition on acetone vaporization at $z/H = 1$: (a) radial profiles of normalized mean vapor concentration for some liquid compositions (from top to bottom, 20%, 40%, 60%, 80% and 100% acetone) and (b) increase of the evaporation rate of acetone at $x/H = 0$, as a function of initial acetone mass fraction.

Figure 12 (a) shows some radial profiles of acetone vapor concentration normalized by C_∞ for some initial acetone mass fraction $Y_{acetone}$ in the droplets. As in Fig. 10, the profiles of the bi-component cases are consistently above that of the mono-component case; moreover, the lower $Y_{acetone}$ the higher the relative concentration profile, meaning that the evaporation rate is even stronger as $Y_{acetone}$ is low.

Figure 12 (b) shows at $z/H = 1$ the evolution of the axial acetone vapor concentration C_{axis} relative to that of the mono-component case ($C_{axis,100\%}$) and normalized by the droplets' initial acetone mass fraction $Y_{acetone}$ (to better compare the relative effect of fuel composition), as a function of $Y_{acetone}$. Again, the lower the initial acetone mass fraction in the droplet, the higher the relative axial concentration: a dilution as high as 90% results in an evaporation rate raised by 56%. The analysis of these results is in progress. Several explanations can be considered:

- The vaporization of pure acetone droplets may be blocked if local saturation conditions are reached. However, analysis of the highest vapor concentrations in the vicinity of the cluster of drops shows no saturation effect.
- The addition of alcohol in the composition of the mixture changes the liquid properties and the evaporation of acetone rate may change. A study is underway concerning the physical properties of the liquid mixture.
- Inside an evaporating bi-component droplet, recent studies showed that the concentration of the components is not homogeneous (**?**). The gradient of acetone concentration inside the drop could cause an over-concentration of acetone in the vicinity of the interface, thereby increasing the acetone evaporation rate.

5. CONCLUSIONS

An experimental study was conducted on the evaporation of a polydispersed bi-component acetone/ethanol droplet mist in highly turbulent conditions, and compared with pure acetone droplets to evaluate the impact of the addition of ethanol in the fuel mixture.

A dedicated test bench was used to generate in a channel an intense turbulent flow of heated air with isotropic and homogeneous behavior. Turbulence levels reach around 25% at the beginning of the established zone, where the spray (droplet Sauter mean diameter $d_{32} = 27$ µm) is produced by means of an air-blast atomizer. Planar Laser-Induced Fluorescence was used to study the vaporization process of droplets in the two-phase flow. An ad-hoc post-processing of the fluorescence images enabled to extract acetone concentration fields along the channel from them.

Results showed that the two-phase flow has a behavior similar to what is observed in the development of free jets concerning the mean radial profiles of acetone vapor concentration, with fluctuations remaining very high (above 33% of C), meaning that the mixing is not perfectly realized in the channel. The evaporation process is fast since 40% of the injected acetone was vaporized by $z/H = 1$.

In addition, it was put in evidence that for a liquid mixture (50% acetone, 50% ethanol) the relative acetone vapor concentration was higher at any given location in the channel than for a pure acetone droplets case, showing that the addition of ethanol in the fuel mixture accelerates the evaporation rate of acetone. In the early development zone of the spray ($z/H = 1$), the effect of alcohol dilution has been studied and showed that a high dilution of 90% resulted in an evaporation rate boosted by more than 50%.

Moreover, turbulent dispersion may lengthen the flight path of droplets with small Stokes numbers, giving them more time to vaporize than larger droplets at a given axial position. Hence, given that pure acetone droplets shrink faster than bicomponent droplets, they should be more affected and/or affected more rapidly by turbulence, which could explain partially the effect observed and described in the present paper.

Yet, the causes of this effect are not well understood yet; the analysis is in progress and several tracks are considered to explain this phenomenon, which is an important step towards a better understanding of multi-component droplets' evaporation modeling.

ACKNOWLEDGMENTS

This work is supported by a grant from Fondation Airbus Group. The authors wish to thank M. Marchal, S. Cazin, C. Korbuly, J.-M. Sfedj and F. Colombiès for their helpful support.

NOMENCLATURE

C	concentration	[g/m^3]	x	radial coordinate	[m]
d	droplet diameter	[m]	y	radial coordinate	[m]
H	channel width	[m]	Y	mass fraction	
I	laser energy	[J]	z	longitudinal coordinate	[m]
$\dot{m}$	mass flow rate	[g/s]	λ	wavelength	[m]
N	number density	[m^{-3}]	σ	absorption cross section	[m^2]
P	pressure	[Pa]	ϕ_λ^f	fluorescence quantum yield	
S_f	signal intensity				
St	Stokes number			**subscripts**	
T	temperature	[K]	axis	on longitudinal axis	
V	radial carrier flow velocity	[m/s]	liq	liquid	
W	axial carrier flow velocity	[m/s]	vap	vapor	

REFERENCES

Ammigan, K., Miller, R., and Clack, H., "Effect of asymmetric radiant heating on monodisperse acetone/ethanol and acetone/2-propanol bi-component droplets," *International Journal of Multiphase Flow*, 38, pp. 67–72, (2012).

Bazile, R. and Stepowski, D., “Measurements of vaporized and liquid fuel concentration fields in a burning spray jet of acetone using planar laser-induced fluorescence,” *Experiments In Fluids*, 20, pp. 1–9, (1995).

Bédat, B. and Cheng, R. K., “Experimental study of premixed flames in intense isotropic turbulence,” *Combustion and Flame*, 100, pp. 485–494, (1995).

Bodoc, V., Multicomponent droplet vaporization, PhD thesis, ONERA DMAE, CERFACS, (2011).

Bodoc, V., Rouzaud, O., and Lavergne, G., “Large eddy simulation of a monocomponent spray evaporating in a heated and turbulent flow,” *Comptes Rendus Mécanique*, 341, pp. 65–74, (2013).

Cochet, M., Bazile, R., Ferret, B., and Cazin, S., “Evaporation of polydispersed droplets in a highly turbulent channel flow,” *Experiments in Fluids*, 47, pp. 379–394, (2009).

Fukushima, C., Aanen, L., and Westerweel, J., “Investigation of the mixing process in an axisymmetric turbulent jet using piv and lif,” *Proceedings of the 10th international symposium on applications of laser techniques to fluid mechanics, Lisbon, Portugal, Paper*, Vol. 11, (2000).

Lazaro, B. J. and Lasheras, J. C., “Particle dispersion in a turbulent, plane, free shear layer,” *Physics of Fluids A-fluid Dynamics*, 1, pp. 1035–1044, (1989).

Maqua, C., Castanet, G., and Lemoine, F., “Bicomponent droplets evaporation: Temperature measurements and modelling,” *Fuel*, 87, pp. 2932–2942, (2008).

Moreau, F. and Bazile, R., “Evaporation of bi-component droplets in a heated, highly turbulent flow,” *Experiments in Fluids*, 53, pp. 331–342, (2012).

Spalding, D. B., “Combustion of fuel particles.,” *Fuel*, 30, pp. 121:130, (1951).

Thurber, M. and Hanson, R., “Pressure and composition dependences of acetone laser-induced fluorescence with excitation at 248, 266, and 308nm,” *Applied Physics B*, 69, pp. 229–240, (1999).

Videto, B. D. and Santavicca, D. A., “A turbulent-flow system for studying turbulent combustion processes,” *Combustion Science and Technology*, 76, pp. 159–164, (1991).